Regular Article

Structure-regulated Ru particles decorated P-vacancy-rich CoP as a highly active and durable catalyst for NaBH$_4$ hydrolysis

Shuqing Zhou [a,1], Yuting Yang [a,1], Wanyu Zhang [a], Xianfa Rao [b], Puxuan Yan [a], Tayirjan Taylor Isimjan [c], Xiulin Yang [a,*]

[a] Guangxi Key Laboratory of Low Carbon Energy Materials, School of Chemistry and Pharmaceutical Sciences, Guangxi Normal University, Guilin 541004, China
[b] School of Resources and Environmental Engineering, Jiangxi University of Science and Technology, Ganzhou 341000, China
[c] Saudi Arabia Basic Industries Corporation (SABIC) at King Abdullah University of Science and Technology (KAUST), Thuwal 23955-6900, Saudi Arabia

HIGHLIGHTS

- Ru-cluster decorated P-vacancy-rich CoP is fabricated by a controllable method.
- The Ru$_{9.8}$/r-CoP catalyst exhibits high activity and reusability for NaBH$_4$ hydrolysis.
- Abundant P vacancies contribute to the formation of more uniform and smaller Ru clusters.
- The superior performance attributed to the synergy of Ru clusters and CoP support.

GRAPHICAL ABSTRACT
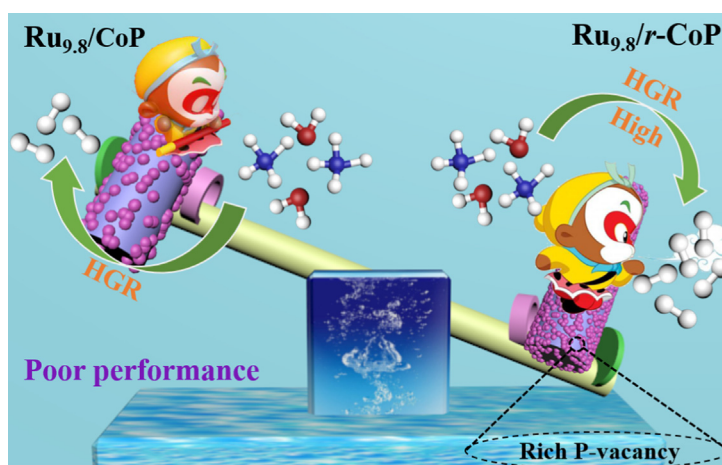
ARTICLE INFO

ABSTRACT

NaBH$_4$ is considered the best hydrogen storage material due to its high hydrogen content of 10.6 wt% and good stability. However, NaBH$_4$ hydrolysis requires an efficient catalyst because of the sluggish reaction kinetics. In this work, we have demonstrated a process of preparing a cobalt phosphide-supported Ru particulate nanocatalyst with abundant phosphorus vacancies for the first time. Electron paramagnetic resonance and transmission electron microscopy revealed that the synthesized Ru$_{9.8}$/r-CoP catalyst has ample phosphorus vacancies, and Ru species are small particles (~2.5 nm) with uniform dispersion, respectively. More importantly, the optimized Ru$_{9.8}$/r-CoP catalyst has the lowest activation energy (45.3 kJ mol^{-1}) and exhibits excellent catalytic performance for NaBH$_4$ hydrolysis with a high hydrogen generation rate 9783.3 mLH$_2$ min^{-1} g$_{cat}^{-1}$ at 25 °C, which is higher than most of the cobalt-based catalysts. Moreover, the Ru$_{9.8}$/r-CoP catalyst also shows good reusability. For example, the catalytic performance only declined by *ca.* 14% after five cycles. The excellent catalytic performance of Ru$_{9.8}$/r-CoP is attributed to the abundant phosphorus vacancies along with a large specific surface area of r-CoP, which makes the Ru particles smaller and more uniformly dispersed on the surface, thereby exposing more active sites to show improved performance.

© 2021 Elsevier Inc. All rights reserved.

* Corresponding author.
  E-mail addresses: isimjant@sabic.com (T.T. Isimjan), xlyang@gxnu.edu.cn (X. Yang).
[1] These authors contributed equally.

1. Introduction

The overconsumption of fossil energy and the increasing attention to environmental issues have prompted researchers to actively seek renewable energy to replace traditional fossil fuels [1,2]. Hydrogen energy is considered to be a promising energy carrier due to its relatively high energy density, environmental friendliness, and potential use in energy conversion devices [3,4]. Among various hydrogen storage materials, NaBH$_4$ is considered the best hydrogen storage material due to its high hydrogen storage content of 10.6 wt%, high purity of hydrogen collected, good stability at room temperature, safe and easy to prepare [5,6]. Most importantly, recent achievements on an economical method of regenerating NaBH$_4$ resolved the biggest hurdle in large-scale applications [7,8]. Due to the slow self-decomposition of NaBH$_4$, the hydrogen production from NaBH$_4$ requires efficient catalysts to promote the reaction rate. In the past, the main focus is on the noble metal-supported catalysts including Ru [9,10], Pt [11,12], Pd [13], and Rh [14] because of the high efficiency and durability. However, with the lack of natural reserves and the high cost of such catalysts, the target is gradually shifted to the synthesis of hybrid catalysts containing both noble and transition metal while keeping the similar activity and durability as pure-noble metal catalysts [15–17].

Furthermore, the metal catalysts are generally supported by silicon carbide [18,19] and carbon nanotubes [20–22]. Although the support could effectively dilute the precious metal content and lower the cost, the interaction between the two species is relatively week, resulting in poor performance, thus requires high metal concentration (~5 wt%) [23]. Recently, the first-row (3d) transition metal phosphides have attracted increasing attention because of their good activity, low cost, and multi-functionality [24–27]. Additionally, the phosphorus vacancies adjust the electronic state of metal phosphides, and regulate the interaction with noble metal particles, thereby optimizing the activation energy of the intermediate catalytic state to improve the catalyst performance [28,29]. For example, Huang et al. reported a highly efficiency CoMoP catalyst for hydrogen generation. The DFT results reveal that the outstanding HER performance results from P defect in CoMoP, preventing the active site blockage from OH* [30]. We assume that a similar approach should also positively affect the NaBH$_4$ hydrolysis catalyst since both catalysts involve hydrogen production and go through a similar mechanism [31]. To the best of our knowledge, we could not find a report related to this topic. As a result, we attempted to construct phosphorus vacancies in cobalt phosphide to regulate the interaction between the noble metal particles and improve its catalytic performance of NaBH$_4$ for hydrogen evolution, hoping to achieve a high-efficiency catalyst with a small quantity of precious metal.

In this work, we have synthesized a reduced three-dimensional (3D) porous cobalt phosphide nanorods with abundant phosphorus defects by employing a facile reduction method. The effect of "killing two birds with one stone" is presented by this reduction method. The Ru loaded cobalt phosphide exhibited excellent activity and stability with a significantly low Ru loading. The crystal structure, phosphorus vacancies, microscopic morphology, and chemical state of the composites are characterized in detail. The NaBH$_4$ hydrolysis test shows that the designed Ru$_{9.8}$/r-CoP catalyst has a high HGR (9783.3 mL$_{H2}$ min^{-1} g$_{cat}^{-1}$), turnover frequency (450.3 mol$_{H2}$ min^{-1} mol$_{Ru}^{-1}$), and good reusability. The excellent performance is attributed to a large number of phosphorus vacancies, the high surface area provided by r-CoP, contributing to the high dispersion of Ru particles and the synergy between them.
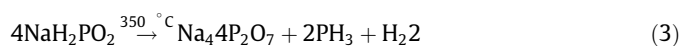
2. Experimental

2.1. Preparation of rod-shaped of CoOOH

All chemicals are of analytical grade and do not require further purification. A typical procedure is as follows: Co(CH$_2$COO)$_2$·4H$_2$O (0.71 g), CH$_3$COONa·3H$_2$O (0.82 g), and PVP (0.10 g) were added into a 100 mL glass beaker with 60 mL of deionized water. The mixture was sonicated and stirred for 30 min. Then, the resulted homogeneous solution was transferred into a 100 mL Teflon-lined autoclave in an oven at 120 °C for 12 h. After that, the precipitates were collected and washed by deionized water and ethanol several times. Finally, the samples were dried in a vacuum oven at 60 °C overnight to obtain a pink powder. The possible reactions can be expressed as follows [32]:

$$Co^{2+} + 2OH^- \xrightarrow{120\ ^\circ C} Co(OH)_2 \tag{1}$$

$$4Co(OH)_2 + O_2 \xrightarrow{120\ ^\circ C} 4CoOOH + 2H_2O \tag{2}$$
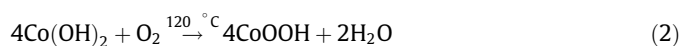
2.2. Preparation of CoP

In a typical preparation of CoP, the CoOOH powder (0.08 g) was located in the middle of a quartz tube with NaH$_2$PO$_2$ (1.0 g) at the upstream side near the CoOOH precursor. The sample was subsequently heated to 350 °C with a rate of 5 °C min^{-1} and kept for 2 h under a N$_2$ atmosphere. After the phosphidation, the samples were cooled down to ambient temperature in flowing N$_2$ gas. The possible reactions are described as follows [33]:

$$4NaH_2PO_2 \xrightarrow{350\ ^\circ C} Na_4 4P_2O_7 + 2PH_3 + H_2 2 \tag{3}$$

$$CoOOH + PH_3 \xrightarrow{350\ ^\circ C} CoP + 2H_2O \tag{4}$$

2.3. Preparation of reduced cobalt phosphide

Briefly, 0.10 g CoP was dispersed in 40 mL 1.5 M NaBH$_4$ solution (or 1.0 M, 2.0 M, and 0.08 M NaBH$_4$ solutions) and stirred at room temperature for 2 h. Then, the products were collected and washed by deionized water and ethanol several times, finally, the samples were dried in a vacuum oven at 60 °C overnight and marked as r-CoP (or r_1-CoP、r_2-CoP and r_3-CoP).

2.4. Preparation of Ru-species/r-CoP

Typically, the r-CoP (30.0 mg) was added into a 50 mL glass beaker with 20.0 mL of deionized water and 12.0 mg (or 6.0, 9.0, 15.0 and 18.0 mg) of RuCl$_3$. The mixed solution was stirred at room temperature for 4 h, then 5 mL (0.08 M) NaBH$_4$ solution was slowly added dropwise, and stirring continued for 0.5 h. The products were collected and washed by deionized water and ethanol several times. Subsequently, the samples dried in a vacuum oven at 60 °C for 12 h. The catalysts are labeled according to the Ru species' actual contents determined by ICP-AES (Table S1). For instance, the Ru$_{9.8}$/r-CoP represents the sample with 9.8 wt% Ru. The Ru content was altered by changing the RuCl$_3$ amounts in the precursor.

2.5. Catalytic hydrolysis of NaBH$_4$ measurements

The catalytic performance of catalytic materials is evaluated by the following test methods: To a 50 mL mixed solution containing 150 mM NaBH$_4$ and 0.4 wt% NaOH was added 10 mg catalyst under vagrous stirring at 25 °C. The classical water-displacement

technique is used to measured the generated H_2, and the drainage system is connected to a computer to record instantaneous water volume changes. During the reusability study, the catalyst was collected by centrifugation and dried. The collected catalyst from the previous experiment was added to the fresh $NaBH_4$ solution in the next experiment. The catalyst's activation energy was tested in the temperature range from 298 to 318 K, and then calculated by the Arrhenius equation. All tests are repeated three times to ensure reliable results.

The hydrogen generation rate (HGR) and turnover frequency (TOF) values are calculated according to the following equations [34,35],

$$HGR = \frac{V_{H_2O}(mL)}{t(\min) \times m(g)} \qquad (5)$$

$$TOF = \frac{n_{H_2}(mol)}{t(\min) \times n_{Ru}(mol)} \qquad (6)$$

where V_{H2O} is the volume of drained water, m is the total mass of the catalyst, n_{H2} is the moles of generated H_2, n_{Ru} is the moles of Ru in the catalyst, and t is the total reaction time in minutes.

$$\ln\kappa = \ln A - E_a/RT \qquad (7)$$

Equation (7) is the Arrhenius equation, where κ (L min^{-1} g^{-1}) is the hydrogen evolution slope, A (L min^{-1} g^{-1}) is a constant, E_a (kJ mol^{-1}) is the activation energy, R (J mol^{-1} K^{-1}) is the gas constant, and T (K) is the temperature of the during the test.

3. Results and discussion

The synthetic processes of the Ru/r-CoP are illustrated in (Fig. 1a). The CoOOH nanorods were first synthesized by low-temperature hydrothermal methods using cobalt acetate and sodium acetate as precursors combined with PVP as a soft template. The CoOOH precursor template was then placed in a quartz boat and phosphorized in a nitrogen atmosphere at a relatively low temperature of 350 °C. The P vacancies were generated by dispersing the as prepared CoP nanorods into $NaBH_4$ solution (1.5 M). The highly reductive condition generates r-CoP with a large number of phosphorus vacancies. The r-CoP was redispersed in $RuCl_3$ solution, and then the $NaBH_4$ solution (0.08 M) was added dropwise to reduce the Ru^{3+} to form Ru/r-CoP.

As shown in (Fig. 1b), the nanorod-shaped CoOOH was synthesized by low-temperature hydrothermal method (the inset is the SEM with different magnifications). After phosphorized, the morphology of CoP still maintained the original rod-like characteristics (Fig. 1c). However, the surface of r-CoP became rough and porous (Fig. 1d) after treatment with $NaBH_4$ solution. As shown in Fig. 1e and f, the Ru/r-CoP and r-CoP show similar morphology and the Ru particles are uniformly dispersed on the surface of r-CoP (the red circle indicates the position of the Ru particles). The statistical results of about 200 Ru particles concluded that the average particle size is approximately 2.52 nm (Fig. S1 and inset Fig. 1f). In contrast, the Ru particles show an apparent agglomeration on $Ru_{9.8}$/CoP (Fig. 1g). The result indicates that higher surface area and porosity help to disperse the Ru ions thereby prevent the agglomeration during reduction. The high-resolution TEM (HRTEM) image (Fig. 1h) further confirmed the crystal structure of the $Ru_{9.8}$/r-CoP whereas the CoP nanorods show two clear lattice spacing of 0.20 and 0.37 nm, corresponding to the crystal planes of (2 1 0) and (1 0 1) [36]. Besides, the other two lattice fringes at 0.22 and 0.19 nm are attributed to the (2 1 0) and (1 0 1) crystal planes of the chemically deposited RuO_2 species, respectively [37] indicating the Ru particles were oxidized upon exposure to the air. The high-angle annular dark-field (HAADF) TEM mapping shows that Ru, Co,

P, and O elements are evenly distributed throughout the $Ru_{9.8}$/r-CoP (Fig. 1i).

X-ray diffraction (XRD) pattern is used to explore the crystal structure of different composite materials. As shown in Fig. S2, the crystal structure of the Co-species prepared by the hydrothermal method is consistent with the standard CoOOH diffraction peak [38]. After phosphorization (Fig. 2a), the XRD patterns of the prepared sample are well-matched with the typical CoP diffraction peaks (JCPDS: 29-0497) [39]. Meanwhile, the r-CoP diffraction peaks are consistent with CoP and indicate that a $NaBH_4$ reduction does not affect the crystal structure of the material. Notably, the XRD peak intensity of $Ru_{9.8}$/r-CoP becomes weaker after the reduction and Ru loading. Fig. 2b shows five-strong Raman scattering peaks at 190, 467, 510, 601, and 668 cm^{-1} of all the samples, corresponding to the distinct regions of cobalt oxide, which may be caused by the oxidation of CoP in the air [40].

Furthermore, it is reported that P vacancies generated by $NaBH_4$ treatment [30,31] accelerate the electron transport during the reaction, thereby accelerating the hydrogen evolution process of $NaBH_4$ [41]. We first studied the effect of different concentrations of $NaBH_4$ on the generation of P vacancies. EPR spectrum found that the most substantial unpaired electron peak was produced when $NaBH_4$ concentration was 1.5 M, suggesting that the largest proportion of P vacancies can be generated at g = ~2.08 (Fig. S3). After the Ru-species were modified (Fig. 2c), the EPR intensity was somewhat weakened, which may be due to the Ru-species occupying some of the P defect sites.

The BET specific surface area of $Ru_{9.8}$/r-CoP, r-CoP, and CoP are calculated to be 71.1, 39.6, and 6.6 m^2 g^{-1} (Fig. 2d), along with the adsorption average pore diameters are about 3.48, 3.51, and 2.24 nm, respectively [42]. Compared with CoP, the r-CoP has a larger BET surface area and porosity, which can disperse Ru particles more uniformly. The $Ru_{9.8}$/r-CoP catalyst exhibits the largest BET surface area resulting in smaller Ru particles and more uniform dispersion, consequently providing more active sites and accelerating the transport of solutes and gas emissions compared to other catalysts, thereby improving catalytic performance [43,44].

To understand the catalyst's electronic state changes, we performed XPS characterization (Fig. 3). The XPS full spectra of the catalysts in Fig. S4 indicate the presence of C, O, P, Co, and/or Ru elements, which are consistent with theoretical values. The high-resolution XPS spectra of C 1 s + Ru 3d regions (Fig. 3a) are convoluted into C—C (284.8 eV) and C—O (286.0 eV) used as calibration standards [45,46], and the Ru 3d core levels from $Ru_{9.8}$/r-CoP and $Ru_{9.8}$/CoP are convoluted at the binding energies of 281.1 eV, 282.3 eV (Ru 3$d_{5/2}$) and 285.5 eV, 286.7 eV (Ru 3$d_{3/2}$) [47,48]. It can be seen that the area ratio of RuO_2 in r-CoP is increased to 73.7% by comparison with CoP (28.2%). The catalyst with a higher RuO_2 content showed a better reaction rate similar to that reported in the recent literature [49,50], revealing that the $NaBH_4$ hydrolysis reaction-rate could be improved significantly through the synergy between the Ru and RuO_2 species in the catalyst. As shown in Fig. 3b, the Co 2$p_{3/2}$ regions' peaks at 778.7, 781.6, and 787.1 eV can be ascribed to the Co–P, Co–O, and satellite peak, respectively [51–53]. Notably, except for CoP that has an obvious Co-P peak, all other catalysts' Co-P peaks become so weak that they are not detectable. This result may be because the oxide layer (r-CoP, $Ru_{9.8}$/CoP, and $Ru_{9.8}$/r-CoP) formed on the catalyst's surface that is thicker than the penetration depth of XPS (about 10 nm). It should be emphasized that we can see clear CoP characteristic peaks in the XRD diffraction spectrum (Fig. 2a), which further proves that only the sample surface is oxidized. The existence of such an oxide layer may be one of the reasons for the formation of more homogeneously dispersed RuO_2 species on the surface of r-CoP. The P 2p regions' peaks at 130.29 and 133.79 eV can be
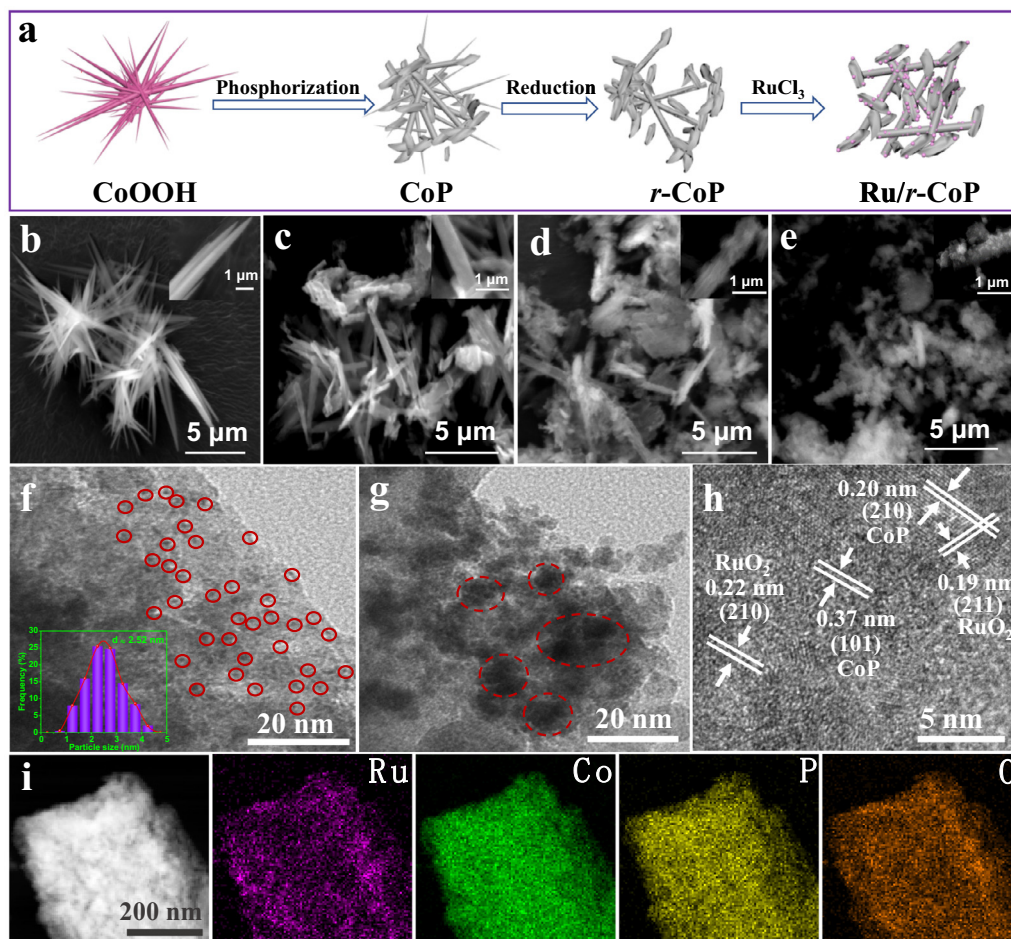
Fig. 1. (a) Fabricating procedure of Ru/*r*-CoP. SEM images of (b) CoOOH, (c) CoP, (d) *r*-CoP, and (e) Ru$_{9.8}$/*r*-CoP. TEM images of (f) Ru$_{9.8}$/*r*-CoP and (g) Ru$_{9.8}$/CoP. HRTEM images of (h) Ru$_{9.8}$/*r*-CoP and elemental mappings of (i) Ru, Co, P and O.

ascribed to the Metal–P and P—O peak (Fig. 3c), respectively [54,55].

The H$_2$ production of NaBH$_4$ hydrolysis using the prepared catalysts was carried out in an alkaline NaBH$_4$ solution at 25 °C. The schematic diagram of the catalytic hydrolysis device is shown in Fig. S5. Where the amount of H$_2$ produced is calculated based on the weight of the water replaced by H$_2$. The self-hydrolysis of NaBH$_4$ has also been studied. When only 150 mM NaBH$_4$ solution is present, very little H$_2$ gas is produced (Fig. S6). However, when an additional 0.4 wt% NaOH is introduced, almost no gas is detected, indicating that NaBH$_4$ is very stable under an alkaline environment (Fig. S7). Moreover, the Ru content of different catalysts was determined by ICP-AES (Table S1), which were 4.5, 5.7, 9.8, 12.5, and 13.4 wt%, respectively. The correlation between the amounts of hydrogen produced with Ru loadings is shown in Fig. 4a. The change of HGR is volcanic. When the content of Ru is 9.8 wt%, the HGR has a maximum value of 9783.3 mL min^{-1} g$_{catalyst}^{-1}$, and the TOF is 450.1 mol min^{-1} mol$_{Ru}^{-1}$ (Fig. 4b), which is one of the highest TOF and HGR currently reported in the literature (Table S3). The excellent catalytic performance can be attributed to the abundant phosphorus vacancies, uniformly dispersed the Ru-species, thereby exposing more active sites. To explore the influence of NaBH$_4$ concentration on the rate of hydrogen evolution, we used different gradient concentrations of NaBH$_4$. Fig. 4c shows that with the increase of NaBH$_4$ concentration, the HGR is almost unchanged. The NaOH concentration has a minimum effect on the HGR after a certain level [56]. We observed similar phenom-

ena in this work (Fig. 4d), signifying the stabilizing rules of NaOH [7,57].

To further study the influence of various catalysts on the rate of hydrogen evolution, CoOOH, CoP, *r*-CoP, Ru$_{9.8}$/CoP, and Ru$_{9.8}$/*r*-CoP were investigated. As shown in Fig. 5a and b, CoOOH, CoP, and *r*-CoP show low hydrolysis activity towards NaBH$_4$ (Note: These TOF values are calculated from the Co content obtained by the ICP-AES test as shown in Table S2). When the Ru loading is 9.8 wt%, Ru$_{9.8}$/*r*-CoP shows the highest hydrogen evolution rate and the highest TOF. The results show that loading a small amount of Ru can significantly increase the HGR of NaBH$_4$ hydrolysis. To measure the activation energy, a set of experiments were conducted at different temperatures using the Ru$_{9.8}$/*r*-CoP along with CoP. As shown in Fig. 5c and Fig. S8, as the reaction temperature increases from 298 K to 318 K, the generation rate of H$_2$ increases rapidly. The rate constant (*k*) is calculated from the initial slope of each experiment. As shown in Fig. 5d, the activation energy of Ru$_{9.8}$/*r*-CoP catalyst was calculated to be 45.3 kJ mol^{-1} by the Arrhenius equation (ln *k* *vs.* 1/T), much lower than CoP (56.5 kJ mol^{-1}), which implies that Ru has an enhanced reaction activity to the hydrolysis of NaBH$_4$ to produce H$_2$ [58].

To evaluate the catalyst's reusability, we assessed the optimized Ru$_{9.8}$/*r*-CoP catalyst's stability through a continuous cycle experiment of NaBH$_4$ hydrolysis in an alkaline solution. After each cycle, the catalyst was washed, freeze-dried, and weighed in sequence. The results show that after five consecutive cycles, the catalytic performance of the Ru$_{9.8}$/*r*-CoP is slightly decayed (Fig. 6a and b).
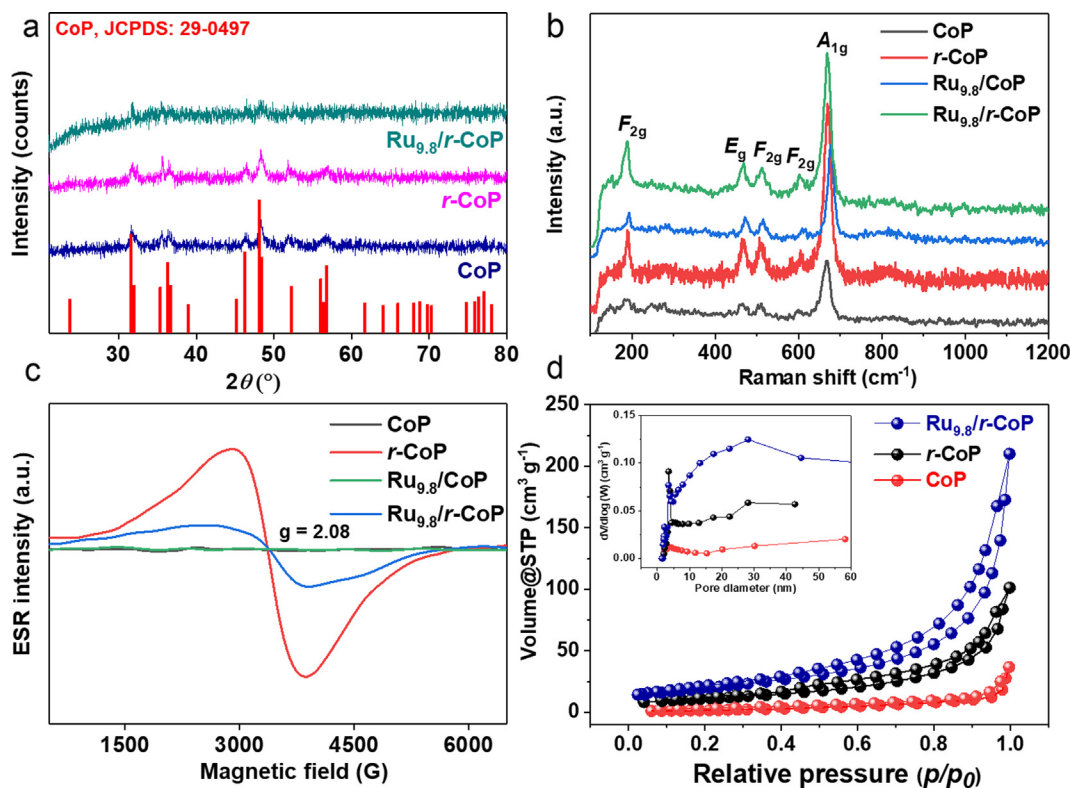
Fig. 2. (a) XRD pattern of CoP, *r*-CoP and Ru$_{9.8}$/*r*-CoP. (b) Raman spectra of CoP, *r*-CoP, Ru$_{9.8}$/CoP and Ru$_{9.8}$/*r*-CoP. (c) EPR spectra of CoP, *r*-CoP, Ru$_{9.8}$/CoP and Ru$_{9.8}$/*r*-CoP. (d) Nitrogen adsorption–desorption isotherms of CoP, *r*-CoP and Ru$_{9.8}$/*r*-CoP.
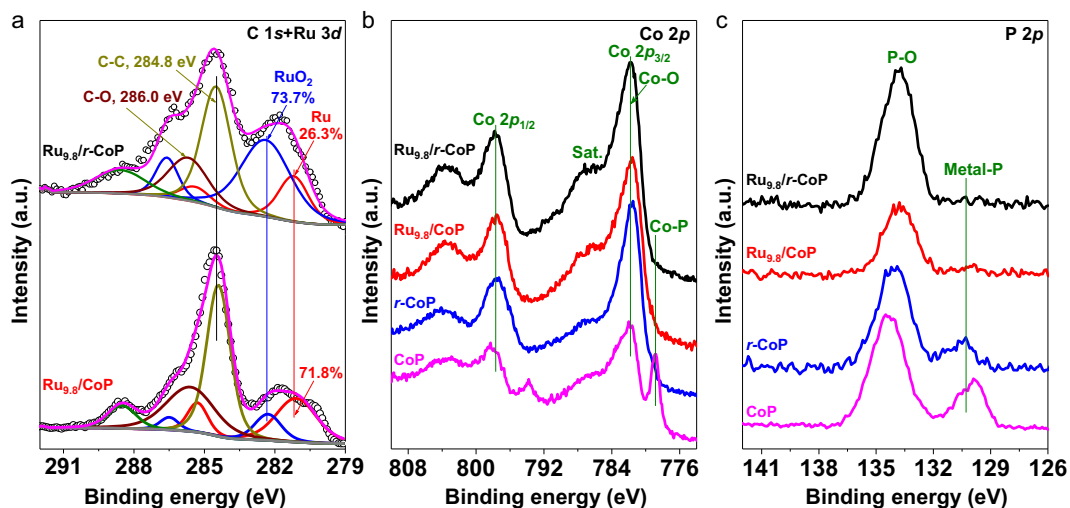

Fig. 3. (a) C 1*s* and Ru 3*d* XPS spectra of Ru$_{9.8}$/CoP and Ru$_{9.8}$/*r*-CoP. (b) Co 2*p* XPS spectra of CoP, *r*-CoP, Ru$_{9.8}$/CoP and Ru$_{9.8}$/*r*-CoP. (c) P 2*p* XPS spectra of CoP, *r*-CoP, Ru$_{9.8}$/CoP and Ru$_{9.8}$/*r*-CoP.

After five cycles, the catalyst remained intact (Fig. S9) and kept the same crystal structure (Fig. S10). However, there is a slight reduction in TOF. However, part of the catalyst deactivation can be attributed to Ru-species exfoliation (Fig. S11) and catalyst poisoning caused by BO_2^- species [59].

The catalytic mechanism diagram of the hydrolysis of NaBH$_4$ solution to hydrogen is proposed in Fig. 6c. The presence of phosphorus vacancies promotes the smaller and more uniformly dispersed Ru particles, consequently increase the grain boundary between the Ru particles and the transition metal phosphide support. Due to the charge transfer from CoP species to Ru resulted from the work function differences (Note: the work functions of Ru is 4.71 eV and CoP is 4.227 eV) [60,61], the Ru becomes electron-rich, thereby selectively binds with B of the BH_4^- ion (Fig. 6c) [62]. Meanwhile, the water is adsorbed by the CoP surface through the P vacancies' binding sites. The adsorbed water molecules can interact with the Ru-BH_4^- at the interface to release one molecule of H$_2$ and form a BH$_3$OH intermediate [63,64]. As the reaction proceeds, the rest of the H atoms in the borohydride are replaced by OH$^-$ ions, ultimately dissociating the B(OH)$_4^-$ species [62].
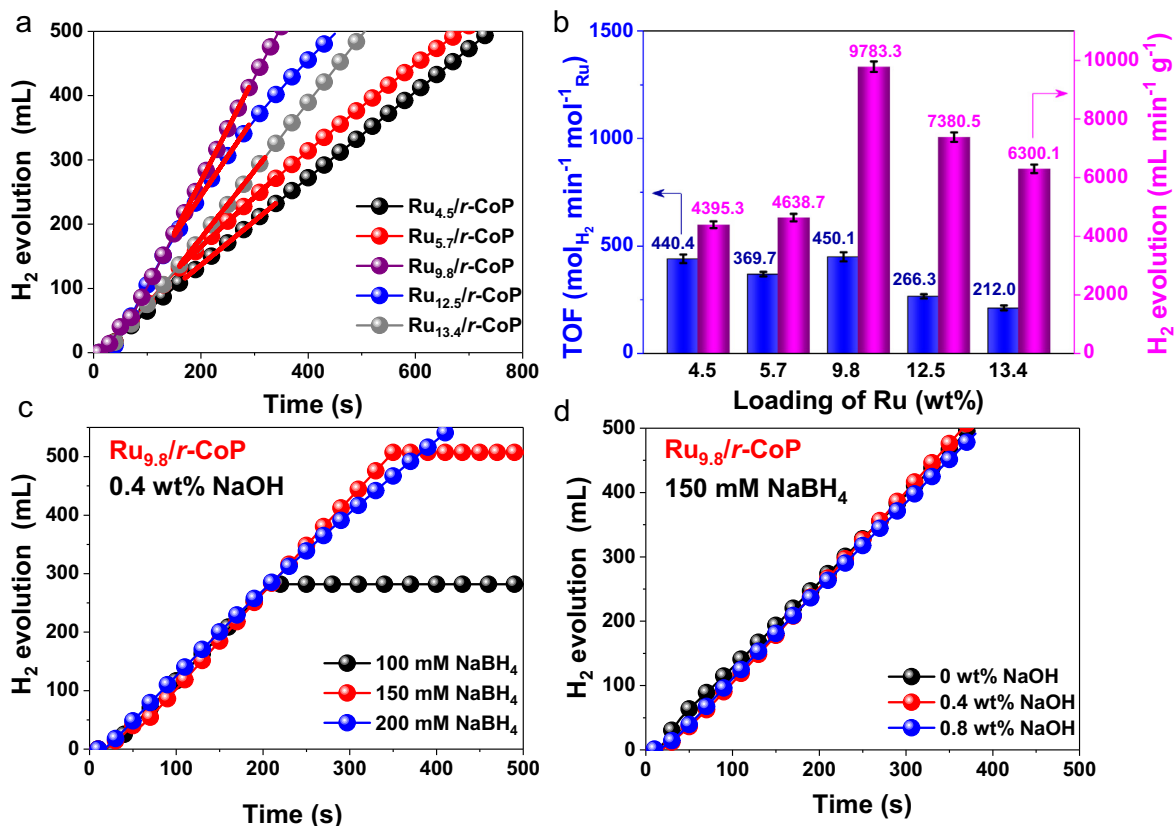
Fig. 4. (a) The relationship between H_2 evolution and loadings of Ru species in Ru_x/r-CoP (x is the mass percentage of Ru) catalysts, and (b) the summarized TOF values and HGR. The influence of $Ru_{9.8}/r$-CoP at (c) different $NaBH_4$ concentrations and (d) different NaOH percentages on $NaBH_4$ hydrolysis to produce H_2.
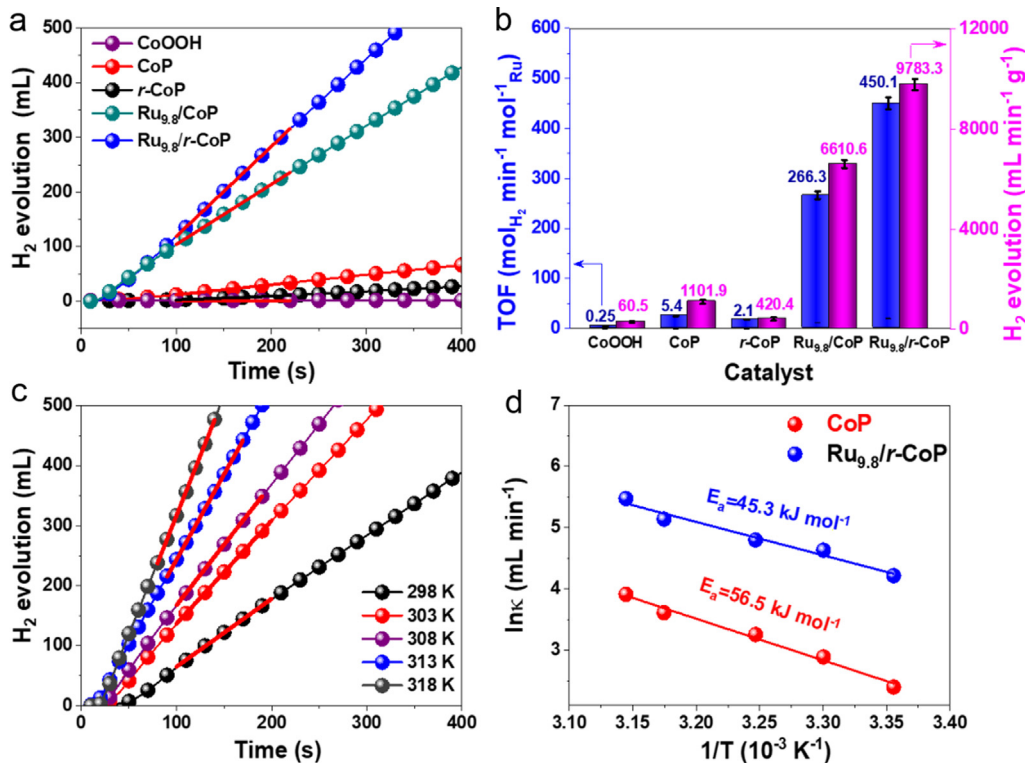

Fig. 5. (a) Different catalyst stoichiometric H_2 evolution, and (b) the corresponding TOF and HGR of the catalyst summarized from a. (c) Stoichiometric H_2 evolution of $Ru_{9.8}/r$-CoP at different reaction temperatures, and (d) the calculated activation energies of $Ru_{9.8}/r$-CoP and CoP catalysts.
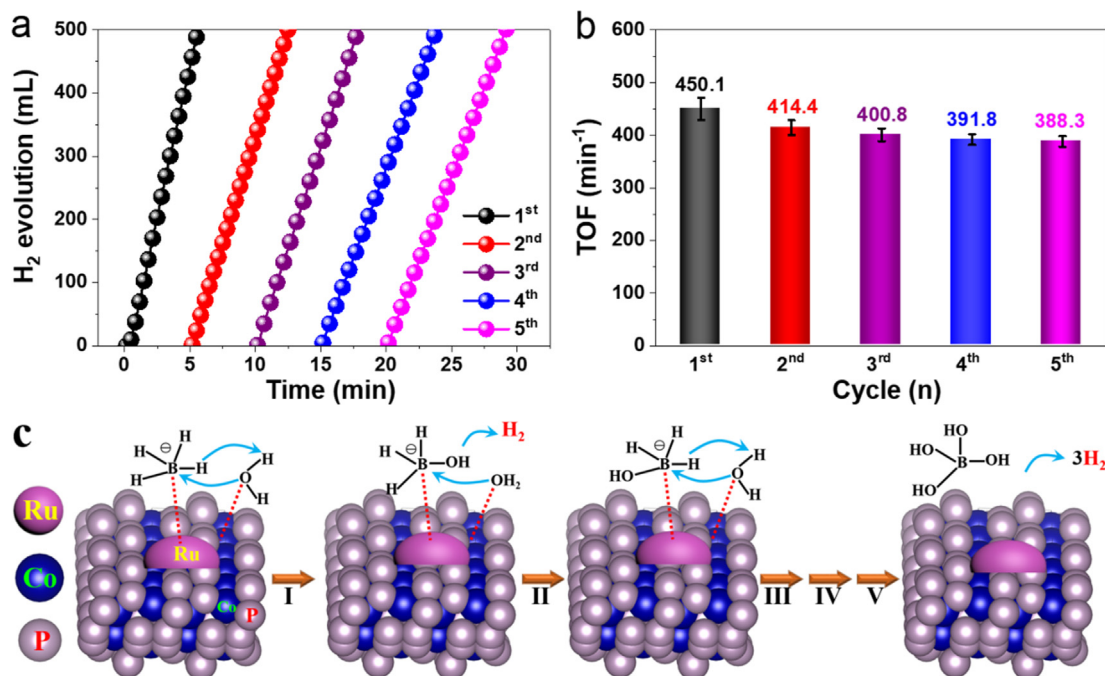
Fig. 6. (a) The stoichiometric H_2 release of the cycle stability test of $Ru_{9.8}/r$-CoP, (b) the corresponding TOF values from a. (c) The proposed catalytic mechanism diagram of $Ru_{9.8}/r$-CoP catalyst generating H_2 by hydrolysis of $NaBH_4$ solution.

4. Conclusions

In summary, we have successfully developed a facile strategy to prepare Ru particles loaded on r-CoP nanorods that produce H_2 by the hydrolysis of $NaBH_4$ in an alkaline solution. EPR, XPS, and TEM analysis of $Ru_{9.8}/r$-CoP material showed that Ru particles were uniformly dispersed on r-CoP nanorods' surface, thereby creating channels for rapid electron transfer, and full exposure of active sites. The superior performance of $Ru_{9.8}/r$-CoP mainly stems from the following facts. Firstly, the reduced cobalt phosphide has a porous 3D nanorod structure, enhanced BET surface area, and specific pore structure, which provides a good platform for the uniform dispersion of Ru particles. Secondly, the *in-situ* generated Ru particles on the r-CoP surface have a smaller particle size and expose more active sites induced by P vacancies, thereby obtaining higher catalytic activity. This research provides a new way to develop metal phosphide based a high-performance and low-loading noble metal catalyst for $NaBH_4$ hydrolysis.

CRediT authorship contribution statement

Shuqing Zhou: Writing - original draft. **Yuting Yang:** Investigation. **Wanyu Zhang:** Data curation. **Xianfa Rao:** Data curation. **Puxuan Yan:** Investigation. **Tayirjan Taylor Isimjan:** Supervision. **Xiulin Yang:** Supervision, Writing - review & editing.

Declaration of Competing Interest

The authors declare that they have no known competing financial interests or personal relationships that could have appeared to influence the work reported in this paper.

Acknowledgements

Appendix A. Supplementary material

Supplementary data to this article can be found online at https://doi.org/10.1016/j.jcis.2021.02.009.

References

[1] S. Demirci, A.K. Sunol, N. Sahiner, Catalytic activity of amine functionalized titanium dioxide nanoparticles in methanolysis of sodium borohydride for hydrogen generation, Appl. Catal. B: Environ. 261 (2020) 118242.

[2] J. Lai, S. Guo, Design of ultrathin Pt-based multimetallic nanostructures for efficient oxygen reduction electrocatalysis, Small 13 (2017) 1702156.

[3] M. Wang, L. Chen, L.C. Sun, Recent progress in electrochemical hydrogen production with earth-abundant metal complexes as catalysts, Energy Environ. Sci. 5 (2012) 6763–6778.

[4] R. Malik, V.K. Tomer, State-of-the-art review of morphological advancements in graphitic carbon nitride (g-CN) for sustainable hydrogen production, Renew. Sust. Energ Rev. 135 (2021) 110235.

[5] N. Selvitepe, A. Balbay, C. Saka, Optimisation of sepiolite clay with phosphoric acid treatment as support material for CoB catalyst and application to produce hydrogen from the NaBH4 hydrolysis, Int. J. Hydrog. Energy 44 (2019) 16387–16399.

[6] H.N. Abdelhamid, A review on hydrogen generation from the hydrolysis of sodium borohydride, Int. J. Hydrogen Energy 46 (2021) 726–765.

[7] Y. Zhu, L. Ouyang, H. Zhong, J. Liu, H. Wang, H. Shao, Z. Huang, M. Zhu, Closing the loop for hydrogen storage: facile regeneration of NaBH4 from its hydrolytic product, Angew. Chem. Int. Ed. 59 (2020) 8623–8629.

[8] H. Zhang, L. Zhang, I.A. Rodríguez-Pérez, W. Miao, K. Chen, W. Wang, Y. Li, S. Han, Carbon nanospheres supported bimetallic Pt-Co as an efficient catalyst for NaBH4 hydrolysis, Appl. Surf. Sci. 540 (2021) 148296.

[9] J. Guo, C. Wu, J. Zhang, P. Yan, J. Tian, X. Shen, T.T. Isimjan, X. Yang, Hierarchically structured rugae-like RuP3–CoP arrays as robust catalysts synergistically promoting hydrogen generation, J. Mater. Chem. A 7 (2019) 8865–8872.

[10] Y. Wang, Z. Liu, Z. Liu, N.T. Suen, X. Yu, L. Feng, Electrochemical hydrogen evolution reaction efficiently catalyzed by Ru2P nanoparticles, ChemSusChem 11 (2018) 2724–2729.

[11] Z. Zhao, C. Chen, Z. Liu, J. Huang, M. Wu, H. Liu, Y. Li, Y. Huang, Pt-based nanocrystal for electrocatalytic oxygen reduction, Adv. Mater. 31 (2019) e1808115.

[12] B.P.G. Guella, A. Miotello, Kinetic features of the platinum catalyzed hydrolysis of sodium borohydride from 11B NMR measurements, J. Phys. Chem. C 111 (2007) 18744–18750.

[13] O. Sahin, D. Kilinc, C. Saka, Hydrogen generation from hydrolysis of sodium borohydride with a novel palladium metal complex catalyst, J. Energy Inst. 89 (2016) 182–189.

[14] Y.V. Larichev, O.V. Netskina, O.V. Komova, V.I. Simagina, Comparative XPS study of Rh/Al$_2$O$_3$ and Rh/TiO$_2$ as catalysts for NaBH$_4$ hydrolysis, Int. J. Hydrog. Energy 35 (2010) 6501–6507.

[15] D.D. Tuan, K.-Y.-A. Lin, Ruthenium supported on ZIF-67 as an enhanced catalyst for hydrogen generation from hydrolysis of sodium borohydride, Chem. Eng. J. 351 (2018) 48–55.

[16] S.A. Al-Thabaiti, Z. Khan, M.A. Malik, Bimetallic Ag-Ni nanoparticles as an effective catalyst for hydrogen generation from hydrolysis of sodium borohydride, Int. J. Hydrogen Energy 44 (2019) 16452–16466.

[17] C. Wu, J. Guo, J. Zhang, Y. Zhao, J. Tian, T.T. Isimjan, X. Yang, Palladium nanoclusters decorated partially decomposed porous ZIF-67 polyhedron with ultrahigh catalytic activity and stability on hydrogen generation, Renew. Energy 136 (2019) 1064–1070.

[18] S. Akbayrak, M. Kaya, M. Volkan, S. Ozkar, Palladium(0) nanoparticles supported on silica-coated cobalt ferrite: A highly active, magnetically isolable and reusable catalyst for hydrolytic dehydrogenation of ammonia borane, Appl. Catal. B: Environ. 147 (2014) 387–393.

[19] S. Akbayrak, M. Kaya, M. Volkan, S. Ozkar, Ruthenium(0) nanoparticles supported on magnetic silica coated cobalt ferrite: Reusable catalyst in hydrogen generation from the hydrolysis of ammonia-borane, J. Mol. Catal. A Chem. 394 (2014) 253–261.

[20] S. Zhang, Y. Ma, L. Suresh, A. Hao, M. Bick, S.C. Tan, J. Chen, Carbon nanotube reinforced strong carbon matrix composites, ACS Nano 14 (2020) 9282–9319.

[21] J. Chen, D.D. Tune, K. Ge, H. Li, B.S. Flavel, Front and back-junction carbon nanotube-silicon solar cells with an industrial architecture, Adv. Funct. Mater. 30 (2020) 2000484.

[22] Y. Hou, Y.L. Liang, P.C. Shi, Y.B. Huang, R. Cao, Atomically dispersed Ni species on N-doped carbon nanotubes for electroreduction of CO$_2$ with nearly 100% CO selectivity, Appl. Catal. B: Environ. 271 (2020) 118929.

[23] J. Chen, Z.-H. Lu, Y. Wang, X. Chen, L. Zhang, Magnetically recyclable Ag/SiO$_2$–CoFe$_2$O$_4$ nanocomposite as a highly active and reusable catalyst for H$_2$ production, Int. J. Hydrog. Energy 40 (2015) 4777–4785.

[24] A. Han, H. Chen, Z. Sun, J. Xu, P. Du, High catalytic activity for water oxidation based on nanostructured nickel phosphide precursors, Chem. Commun. 51 (2015) 11626–11629.

[25] L.A. Stern, L.G. Feng, F. Song, X.L. Hu, Ni$_2$P as a Janus catalyst for water splitting: the oxygen evolution activity of Ni$_2$P nanoparticles, Energy Environ. Sci. 8 (2015) 2347–2351.

[26] J.M. Wang, Z. Liu, Y.W. Zheng, L. Cui, W.R. Yang, J.Q. Liu, Recent advances in cobalt phosphide based materials for energy-related applications, J. Mater. Chem. A 5 (2017) 22913–22932.

[27] C.Z. Yuan, S.L. Zhong, Y.F. Jiang, Z.K. Yang, Z.W. Zhao, S.J. Zhao, N. Jiang, A.W. Xu, Direct growth of cobalt-rich cobalt phosphide catalysts on cobalt foil: an efficient and self-supported bifunctional electrode for overall water splitting in alkaline media, J. Mater. Chem. A 5 (2017) 10561–10566.

[28] X.C. Zhou, H. Gao, Y.F. Wang, Z. Liu, J.Q. Lin, Y. Ding, P vacancies-enriched 3D hierarchical reduced cobalt phosphide as a precursor template for defect engineering for efficient water oxidation, J. Mater. Chem. A 6 (2018) 14939–14948.

[29] Z. Ran, C. Shu, Z. Hou, P. Hei, T. Yang, R. Liang, J. Li, J. Long, Phosphorus vacancies enriched Ni$_2$P nanosheets as efficient electrocatalyst for high-performance Li–O$_2$ batteries, Electrochim. Acta 337 (2020) 135795.

[30] X.K. Huang, X.P. Xu, X.X. Luan, D.J. Cheng, CoP nanowires coupled with CoMoP nanosheets as a highly efficient cooperative catalyst for hydrogen evolution reaction, Nano Energy 68 (2020) 104332.

[31] J. Guo, B. Wang, D. Yang, Z. Wan, P. Yan, J. Tian, T.T. Isimjan, X. Yang, Rugae-like Ni$_2$P-CoP nanoarrays as a bi-functional catalyst for hydrogen generation: NaBH$_4$ hydrolysis and water reduction, Appl. Catal. B: Environ. 265 (2020) 118584.

[32] K.-Y. Niu, L. Fang, R. Ye, D. Nordlund, M.M. Doeff, F. Lin, H. Zheng, Tailoring transition-metal hydroxides and oxides by photon-induced reactions, Angew. Chem. Int. Ed. 55 (2016) 14272–14276.

[33] D. Liu, X. Li, L. Wei, T. Zhang, A. Wang, C. Liu, R. Prins, Disproportionation of hypophosphite and phosphite, Dalton Trans. 46 (2017) 6366–6378.

[34] L. Cui, Y. Xu, L. Niu, W. Yang, J. Liu, Monolithically integrated CoP nanowire array: An on/off switch for effective on-demand hydrogen generation via hydrolysis of NaBH$_4$ and NH$_3$BH$_3$, Nano Res. 10 (2017) 595–604.

[35] Q. Yao, Z.-H. Lu, Y. Yang, Y. Chen, X. Chen, H.-L. Jiang, Facile synthesis of graphene-supported Ni-CeO$_x$ nanocomposites as highly efficient catalysts for hydrolytic dehydrogenation of ammonia borane, Nano Res. 11 (2018) 4412–4422.

[36] C. Cai, Y. Teng, J.H. Wu, J.Y. Li, H.Y. Chen, J.H. Chen, D.B. Kuang, In situ photosynthesis of an MAPbI(3)/CoP hybrid heterojunction for efficient photocatalytic hydrogen evolution, Adv. Funct. Mater. 30 (2020) 2001478.

[37] M. Kuang, Y. Wang, W. Fang, H. Tan, M. Chen, J. Yao, C. Liu, J. Xu, K. Zhou, Q. Yan, Efficient nitrate synthesis via ambient nitrogen oxidation with Ru-doped TiO$_2$/RuO$_2$ electrocatalysts, Adv. Mater. 32 (2020) e2002189.

[38] X.L. Yang, H.N. Li, A.Y. Lu, S.X. Min, Z. Idriss, M.N. Hedhili, K.W. Huang, H. Idriss, L.J. Li, Highly acid-durable carbon coated Co$_3$O$_4$ nanoarrays as efficient oxygen evolution electrocatalysts, Nano Energy 25 (2016) 42–50.

[39] G. Huang, W. Liang, Y. Wu, J. Li, Y.Q. Jin, H. Zeng, H. Zhang, F. Xie, J. Chen, N. Wang, Y. Jin, H. Meng, Co$_2$P/CoP hybrid as a reversible electrocatalyst for hydrogen oxidation/evolution reactions in alkaline medium, J. Catal. 390 (2020) 23–29.

[40] P. Yan, M. Huang, B. Wang, Z. Wan, M. Qian, H. Yan, T.T. Isimjan, J. Tian, X. Yang, Oxygen defect-rich double-layer hierarchical porous Co$_3$O$_4$ arrays as high-efficient oxygen evolution catalyst for overall water splitting, J. Energy Chem. 47 (2020) 299–306.

[41] M. Yang, H. Qi, F. Liu, Y. Ren, X. Pan, L. Zhang, X. Liu, H. Wang, J. Pang, M. Zheng, A. Wang, T. Zhang, One-pot production of cellulosic ethanol via tandem catalysis over a multifunctional Mo/Pt/WO$_x$ catalyst, Joule 3 (2019) 1937–1948.

[42] Y. Yi, W. Zhao, Z. Zeng, C. Wei, C. Lu, Y. Shao, W. Guo, S. Dou, J. Sun, ZIF-8@ZIF-67-derived nitrogen-doped porous carbon confined CoP polyhedron targeting superior potassium-ion storage, Small 16 (2020) 1906566.

[43] H.N. Abdelhamid, Hierarchical porous ZIF-8 for hydrogen production via the hydrolysis of sodium borohydride, Dalton Trans. 49 (2020) 4416–4424.

[44] H.N. Abdelhamid, UiO-66 as a catalyst for hydrogen production via the hydrolysis of sodium borohydride, Dalton Trans. 49 (2020) 10851–10857.

[45] M. Qian, M. Xu, S. Zhou, J. Tian, T. Taylor Isimjan, Z. Shi, X. Yang, Template synthesis of two-dimensional ternary nickel-cobalt-nitrogen co-doped porous carbon film: promoting the conductivity and more active sites for oxygen reduction, J. Colloid Interface Sci. 564 (2020) 276–285.

[46] B. Wang, H. Huang, T. Sun, P. Yan, T.T. Isimjan, J. Tian, X. Yang, Dissolution reconstruction of electron-transfer enhanced hierarchical NiS$_x$-MoO$_2$ nanosponges as a promising industrialized hydrogen evolution catalyst beyond Pt/C, J. Colloid Interface Sci. 567 (2020) 339–346.

[47] H.C. Sun, J.M. Yang, J.G. Li, Z.S. Li, X. Ao, Y.Z. Liu, Y. Zhang, Y. Li, C.D. Wang, J. Tang, Synergistic coupling of NiTe nanoarrays with RuO$_2$ and NiFe-LDH layers for high-efficiency electrochemical-/photovoltage-driven overall water splitting, Appl. Catal. B: Environ. 272 (2020) 118988.

[48] S. Dou, W. Zhang, Y. Yang, S. Zhou, X. Rao, P. Yan, T.T. Isimjan, X. Yang, Shaggy-like Ru-clusters decorated core-shell metal-organic framework-derived CoO$_x$@NPC as high-efficiency catalyst for NaBH4 hydrolysis, Int. J. Hydrogen Energy (2021), https://doi.org/10.1016/j.ijhydene.2020.1012.1011.

[49] Y.-H. Qin, H.-H. Yang, R.-L. Lv, W.-G. Wang, C.-W. Wang, TiO$_2$ nanotube arrays supported Pd nanoparticles for ethanol electrooxidation in alkaline media, Electrochim. Acta 106 (2013) 372–377.

[50] Y. Li, X. Zhang, Q. Zhang, J. Zheng, N. Zhang, B.H. Chen, K.J. Smith, Activity and kinetics of ruthenium supported catalysts for sodium borohydride hydrolysis to hydrogen, RSC Adv. 6 (2016) 29371–29377.

[51] L. Yang, R.M. Liu, L.F. Jiao, Electronic redistribution: construction and modulation of interface engineering on CoP for enhancing overall water splitting, Adv. Funct. Mater. 30 (2020) 1909618.

[52] Z.H. Zou, J.L. Wang, H.R. Pan, J. Li, K.L. Guo, Y.Q. Zhao, C.L. Xu, Enhanced oxygen evolution reaction of defective CoP/MOF-integrated electrocatalyst by partial phosphating, J. Mater. Chem. A 8 (2020) 14099–14105.

[53] Y.P. Li, Y. Liu, Q.Z. Qian, G.R. Wang, G.Q. Zhang, Supramolecular assisted one-pot synthesis of donut-shaped CoP@PNC hybrid nanostructures as multifunctional electrocatalysts for rechargeable Zn-air batteries and self-powered hydrogen production, Energy Storage Mater. 28 (2020) 27–36.

[54] Y. Liu, Y. Zhao, Y. Sun, J. Cao, H. Wang, X. Wang, H. Huang, M. Shao, Y. Liu, Z. Kang, A 4e–2e– cascaded pathway for highly efficient production of H2 and H2O2 from water photo-splitting at normal pressure, Appl. Catal. B: Environ. 270 (2020) 118875.

[55] L. Chai, Z. Hu, X. Wang, Y. Xu, L. Zhang, T.T. Li, Y. Hu, J. Qian, S. Huang, Stringing bimetallic metal-organic framework-derived cobalt phosphide composite for high-efficiency overall water splitting, Adv. Sci. 7 (2020) 1903195.

[56] W. Wang, Y. Zhao, D. Chen, X. Wang, X. Peng, J. Tian, Promoted Mo incorporated Co–Ru–B catalyst for fast hydrolysis of NaBH$_4$ in alkaline solutions, Int. J. Hydrog. Energy 39 (2014) 16202–16211.

[57] Z. Wu, X. Mao, Q. Zi, R. Zhang, T. Dou, A.C.K. Yip, Mechanism and kinetics of sodium borohydride hydrolysis over crystalline nickel and nickel boride and amorphous nickel–boron nanoparticles, J. Power Sources 268 (2014) 596–603.

[58] D. Kılınç, Ö. Şahìn, C. Saka, Salicylaldimine-Ni complex supported on Al$_2$O$_3$: Highly efficient catalyst for hydrogen production from hydrolysis of sodium borohydride, Int. J. Hydrog. Energy 43 (2018) 251–261.

[59] L.M. Zhou, J. Meng, P. Li, Z.L. Tao, L.Q. Mai, J. Chen, Ultrasmall cobalt nanoparticles supported on nitrogen-doped porous carbon nanowires for hydrogen evolution from ammonia borane, Mater. Horiz. 4 (2017) 268–273.

[60] L. Li, Y. Wang, S. Vanka, X. Mu, Z. Mi, C.-J. Li, Nitrogen photofixation over III-nitride nanowires assisted by ruthenium clusters of low atomicity, Angew. Chem. Int. Ed. 56 (2017) 8701–8705.

[61] Q. Liu, J. Huang, H. Tang, X. Yu, J. Shen, Construction 0D TiO$_2$ nanoparticles/2D CoP nanosheets heterojunctions for enhanced photocatalytic H$_2$ evolution activity, J. Mater. Sci. Technol. 56 (2020) 196–205.

[62] U.B. Demirci, P. Miele, Reaction mechanisms of the hydrolysis of sodium borohydride: A discussion focusing on cobalt-based catalysts, C.R. Chim. 17 (2014) 707–716.

[63] A.A. Kassem, H.N. Abdelhamid, D.M. Fouad, S.A. Ibrahim, Metal-organic frameworks (MOFs) and MOFs-derived CuO@C for hydrogen generation from sodium borohydride, Int. J. Hydrogen Energy 44 (2019) 31230–31238.

[64] S. Dou, S. Zhou, H. Huang, P. Yan, E. Shoko, T.T. Isimjan, X. Yang, Metal-Organic Framework (MOF)-derived electron-transfer enhanced homogeneous PdO-Rich Co$_3$O$_4$ as a highly efficient bifunctional catalyst for sodium borohydride hydrolysis and 4-nitrophenol reduction, Chem. Eur. J. 26 (2020) 16923–16931.